

ARTICLE

Received 26 Apr 2016 | Accepted 25 Aug 2016 | Published 4 Oct 2016

DOI: 10.1038/ncomms13015

OPEN

Structure of the *Neisseria meningitidis* Type IV pilus

Subramania Kolappan¹, Mathieu Coureuil², Xiong Yu³, Xavier Nassif², Edward H. Egelman³ & Lisa Craig¹

Neisseria meningitidis use Type IV pili (T4P) to adhere to endothelial cells and breach the blood brain barrier, causing cause fatal meningitis. T4P are multifunctional polymers of the major pilin protein, which share a conserved hydrophobic N terminus that is a curved extended α -helix, α 1, in X-ray crystal structures. Here we report a 1.44 Å crystal structure of the *N. meningitidis* major pilin PilE and a \sim 6 Å cryo-electron microscopy reconstruction of the intact pilus, from which we built an atomic model for the filament. This structure reveals the molecular arrangement of the N-terminal α -helices in the filament core, including a melted central portion of α 1 and a bridge of electron density consistent with a predicted salt bridge necessary for pilus assembly. This structure has important implications for understanding pilus biology.

¹Department of Molecular Biology and Biochemistry, Simon Fraser University, Burnaby, British Columbia, Canada V5A 1S6. ²Institut Necker-Enfants Malades, INSERM U1151, Université Paris Descartes, 14 Rue Maria Helena Vieira Da Silva, CS 61431, 75014 Paris, France. ³Department of Biochemistry and Molecular Genetics, University of Virginia School of Medicine, Charlottesville, Virginia 22908, USA. Correspondence and requests for materials should be addressed to E.H.E. (email: egelman@virginia.edu) or to L.C. (email: licraig@sfu.ca).

N*eisseria meningitidis* (Nm) is one of the very few extracellular bacterial pathogens able to cross the blood brain barrier after having invaded the bloodstream from the nasopharynx. In the bloodstream an unusually tight interaction between the bacteria and the brain microvasculature endothelial cells is established, leading to cortical plaque formation that results in opening of the blood brain barrier and bacterial invasion of the brain^{1–5}. This interaction is mediated by Type IV pili (T4P), long thin polymers of pilin proteins that interact with two endothelial cell receptors, CD147 and the β 2 adrenergic receptor (β 2AR). The interaction with CD147 is responsible for bacterial adhesion⁶ and the interaction with the β 2AR induces signalling in endothelial cells⁷. While the host cell signalling events that lead to disruption of the blood brain barrier are somewhat well-defined, the mechanism by which T4P initiate this process is poorly understood and would benefit from a detailed structure of the *N. meningitidis* T4P.

X-ray crystal structures of full-length Type IV pilin proteins have been obtained by dissociating intact pilus filaments with detergent, revealing a canonical structure with an extended gently curving 53-amino-acid α -helix (α 1), the C-terminal half of which is embedded in a globular C-terminal domain^{8–12}. The N-terminal half of the α -helix, α 1N, protrudes from the globular domain and is comprised of hydrophobic residues, with the exception of a threonine or serine at position 2 and an invariant glutamate at position 5. Two helix-breaking residues, Pro22 and Gly42, which are conserved in Type IV pilins of the IVa class, introduce kinks in α 1 and are responsible for its curvature. An additional glycine at position 14 is also conserved. α 1N has dual functions in T4P biogenesis: it anchors the globular domain in the inner membrane before pilus assembly¹³, and it interacts with adjacent α 1Ns in the assembled pilus, forming a staggered helical array in the filament core^{8,9,14,15}. The conserved Glu5 is critical for T4P assembly^{14,16–22} and models of T4P, based in part on the crystal structure of the full-length pilin subunit from *Neisseria gonorrhoeae*, PilE (Ng PilE), place this side chain in a salt bridge with the positively charged N-terminal amine of its neighbouring molecule in the otherwise hydrophobic core of the filament^{8,9,11,14,23}.

N. meningitidis PilE (Nm PilE) is 78% identical to Ng PilE and 100% identical in α 1 (Fig. 1a,b). Both pilins share a \sim 20 amino-acid hypervariable region, located between two conserved cysteines, imparting antigenic variability to these pili^{24–26}. In *N. gonorrhoeae* PilE the hypervariable region is located on a β -hairpin that lies on top of the globular domain β -sheet^{9,11}. A cryo-electron microscopy (cryoEM) reconstruction of the Ng T4P was determined at 12.5 Å resolution and an atomic model was built by fitting the full-length Ng PilE structure into the cryoEM density⁹. The PilE globular domains fit well into the reconstruction, exposing the hypervariable region prominently on the pilus surface and burying the N-terminal α -helices in the filament core. PilE subunits are related in the Ng T4P reconstruction by an axial rise of 10.5 Å and an azimuthal rotation (twist) of 100.8°. The subunits are held together largely by hydrophobic interactions among the N-terminal α -helices but these helices were not resolved due to the limited resolution cryoEM map. The importance of the hydrophobic interactions was corroborated by biochemical studies, which showed that Ng T4P require detergent to dissociate into pilin subunits^{9,11,14}. The interactions between subunits are very strong, requiring temperatures of 60 °C to denature the filaments¹⁴, consistent with their ability to withstand tensile forces of 100 pN or more^{27–31}. Yet both Ng and Nm T4P have been shown to undergo a force-induced conformational change that exposes an epitope, EYYLN, along the length of the pilus^{29,32}. EYYLN is located at the end of α 1 (residues 49–53) in Ng PilE, a site that is buried by

subunit:subunit interactions in the Ng T4P model and only accessible at the tips of the pili⁹. Consistent with this model, anti-EYYLN antibodies normally bind to the tips of Nm and Ng T4P but not along its length^{33,34}. Yet when Ng T4P are placed under force using optical or magnetic tweezers or molecular combing they become longer and narrower²⁹. This force-induced conformational change exposes the anti-EYYLN epitope all along the length of the pilus, allowing antibody to bind. Similarly, Brissac *et al.* showed that anti-EYYLN antibodies can bind along the length of Nm T4P when Nm are adhered to endothelial cells, a property that is dependent on expression of the minor pilin, PilX³². It is unclear how these T4P extend in a reversible manner without completely disrupting the extensive hydrophobic interactions among the N-terminal α -helices in the core of the filament. Another poorly understood phenomenon of T4P from at least one species, *Geobacter sulfurreducens*, is their ability to facilitate long-range electron transport, a property that is thought to occur via overlapping π - π orbitals of aromatic residues in α 1 (refs 35,36). Higher resolution structures may provide a molecular basis for these and other remarkable properties of T4P.

Here we report the 1.44 Å X-ray crystal structure of Nm PilE and a cryoEM reconstruction of the Nm pilus at higher resolution, \sim 6 Å, than any T4P structure reported previously. Portions of the N-terminal α -helices are clearly resolved in this reconstruction, allowing their precise placement, which provides evidence of a salt bridge between Phe1:N and the Glu5 side chain, and reveals a melting of the central portion of α 1N. This structure provides a molecular framework for understanding key aspects of T4P biology.

Results

Structure of the major pilin PilE from *N. meningitidis*.

N. meningitidis Δ N-PilE, comprising residues 29–161 of PilE from the high adhesive SB variant of *N. meningitidis* strain 8013 (ref. 37) was expressed with an N-terminal His-tag. This PilE variant, when expressed as a maltose-binding protein fusion on *Staphylococcus aureus*, induces recruitment of the β 2AR in endothelial cells³⁸. Δ N-PilE crystals were grown in the P2₁2₁2₁ space group and the structure was solved by molecular replacement with the full-length PilE structure from *N. gonorrhoeae* (Ng PilE, 2H12⁹), which shares 78% sequence identity with *N. meningitidis* PilE (Nm PilE; Fig. 1a). Data collection and refinement statistics are reported in Table 1. Nm Δ N-PilE is a globular protein with an N-terminal α -helix corresponding to α 1C, the C-terminal half of α 1 (Fig. 2a), embedded in a four-stranded antiparallel β -sheet (β 1 to β 4, residues 77–121). Between α 1C and the β -sheet is the $\alpha\beta$ -loop (residues 54–76), an extended segment with a single-turn α -helix and a 3_{10} helix that forms one edge of the globular domain. Two residues in the $\alpha\beta$ -loop, Ser63 and Ser69, are post-translationally modified in the native PilE^{39,40}. On the opposite side of the β -sheet, the polypeptide chain exits β 4 and forms a β -hairpin (β 5– β 6) that lies atop the β -sheet, followed by an irregular segment that protrudes from the globular domain surface then wraps under it, ending in an extended C terminus at the edge opposite the $\alpha\beta$ -loop. Conserved disulfide-bonded cysteines at the end of β 4 (Cys120) and close to the C terminus (Cys154) define the boundaries of the D-region containing the β -hairpin. The most protruding segment of the D-region, the β -hairpin loop and β 6 plus the beginning of the loop that follows β 6, is highly variable in sequence among *N. meningitidis* Type IV pilins and is referred to as the hypervariable region (residues \sim 127 to 146)³⁸. The β -hairpin loop hooks over the top of the β -sheet and across

Table 1 | Nm Δ N-PilE data collection and refinement statistics.

Data collection	Nm Δ N-PilE
Beamline	SSRL 7-1
Wavelength (Å)	0.9753
Space group	P2 ₁ 2 ₁ 2 ₁
Cell <i>a</i> , <i>b</i> , <i>c</i> (Å)	43.5, 46.3, 48.4
Cell α , β , γ (°)	90.0, 90.0, 90.0
Resolution (Å)	1.44
Completeness (%)	98.7 (88.1)*
No. of observed reflections	118934
No. of unique reflections	18088
<i>R</i> _{meas} (%)	6.0 (60.7)
<i>R</i> -factor _{obs}	5.5 (53.9)
<i>I</i> / σ (<i>I</i>)	21.6 (2.8)
Wilson <i>B</i> value (Å ²)	18.7
Mosaicity (°)	0.5
Refinement	
Resolution limits (Å)	33.43-1.44
<i>Z</i>	4
No. of reflections used	18030
<i>R</i> _{cryst} (%)	18.7
<i>R</i> _{free} (%)	21.0
No. of non-hydrogen atoms:	
Protein	1037
Water	156
Avg <i>B</i> factor (Å²):	
Protein	16.5
Water oxygen	24.8
RMSD bond lengths (Å)	0.004
RMSD bond angles (°)	0.679
Ramachandron plot	
Favoured (%)	94.2
Allowed (%)	5.8
Outlier (%)	0
PDB ID	5JW8

RMSD, root mean squared deviation

*Values in parenthesis represent the highest resolution shell.

N-terminal residues in Nm Δ N-PilE monomer are also expected to be α -helical, forming a continuous α -helix with α 1C, as seen in the full-length Ng PilE structure. The conserved Pro22 and Gly42 introduce kinks in Ng PilE, giving α 1 a gentle S-shaped curve (Fig. 2b). Both proteins share essentially the same secondary structure elements in the globular domain (Figs 1a and 2). The only notable main chain deviations are in the position of the β 3– β 4 loop, which bends away from the β -strand in Nm PilE to a greater degree than it does in Ng PilE, and in the β -hairpin, which is more twisted in Nm PilE and has a two-residue insertion in its loop that allows it to contact the $\alpha\beta$ -loop.

CryoEM reconstruction of the *N. meningitidis* T4P. To better understand the role of *N. meningitidis* T4P (Nm T4P) in host cell adhesion and signalling, we generated a cryoEM reconstruction. Not only are the Nm T4P filaments quite flexible, but image analysis indicated substantial variability, mainly in the twist (Methods). The Iterative Helical Real Space Reconstruction (IHRSR)⁴¹ approach was used to obtain the reconstruction, which after sorting converged to a rise of 10.3 Å and a rotation of 100.8° for the subset of segments used. The cryoEM map, with an estimated resolution of ~6 Å, shows well-defined density for the PilE globular domain, with a central depression and a protruding ridge on one side (Fig. 3a). Clear connectivity between the globular domains is observed between subunits in the

right-handed 4-start (+4) helix, and to a lesser extent in the left-handed 3-start (–3) and right-handed 1-start (+1) helices. Rod-like density is present in the core of the filament consistent with the protruding N-terminal α -helical segments of PilE, α 1N (Fig. 3b, c). This density shows that the α 1N segments are staggered in a helical array in the filament core and partially tilted relative to the filament axis, with their N termini close to the centre of the filament and their C termini lying at a larger radius. Surprisingly the α -helical density is not continuous, being considerably weaker just before it connects with the globular domains (red asterisks in Fig. 3c). This weak density indicates loss of α -helical order and increased flexibility in a central segment of α 1 in the intact pilus.

Atomic model of the *N. meningitidis* T4P. As a first step in building an Nm T4P model, the full-length Ng PilE structure was fit as a rigid body into the Nm pilus cryoEM density map to determine a global fit for Nm PilE that included α 1N. While the Ng PilE globular domain, which includes residues ~28–53 of α 1 (α 1C), fits nicely into the map, the kink in α 1N at Pro22 drives the N-terminal end of α 1N well away from the rod-like density corresponding to this subunit (Fig. 3c). Thus, we built a model for the Nm T4P by separately fitting the Nm Δ N-PilE structure (residues 29–161) and α 1N from the full-length Ng PilE structure, separated into two segments, α 1:1–14 and α 1:24–28, into the cryoEM map. These α -helical segments were then joined by an extended non-helical segment, α 1:15–23 (Fig. 3d).

The Nm T4P model was built iteratively as described in Methods. The final model was selected based on its fit to the electron density map, minimal steric clashes between subunits, and close proximity of the Glu5 side chain with the N-terminal amine of Phe1 in adjacent subunits. Refinement statistics are shown in Table 2. The diameter of the Nm T4P reconstruction and filament model is ~60 Å. The Nm Δ N-PilE crystal structure within the pilus model fits nicely into the cryoEM map (Fig. 4a, Supplementary Movie 1), having undergone only minor conformational adjustments during fitting and refinement including movement of the β 3– β 4 loop to bring it into proximity with an adjacent subunit (Fig. 4b). The ridge of density located on one side of the globular domain is occupied by the hypervariable segment of the D-region, the β -hairpin loop, β 6 and the loop following β 6, with Lys140 prominently displayed at its most protruding point. Lys140 is critical for pilus bundling and T4P-mediated bacterial aggregation, a phenotype associated with the high adhesive variant of *N. meningitidis* strain 8013 (ref. 42). The long axes of the globular domains run along the 4-start helix, each strand accentuated by the hypervariable ridges (Fig. 4a). The hypervariable region is implicated in binding to and remodelling of endothelial cells and was predicted based upon homology with Ng PilE to be surface-exposed³⁸. Four key residues on Nm PilE mediate interactions of Nm T4P with β 2AR and activation of endothelial cells: Thr130, Lys140, Asp143 and Lys144 (ref. 38). Thr130 lies on the β -hairpin β 5– β 6 loop near the top of the protruding hypervariable ridge whereas Lys140, Asp143 and Lys144 are located near the bottom of this ridge (Fig. 4a,b). The distance between these two binding sites on one PilE subunit (~26 Å) is approximately equal to the distance between these sites in neighbouring subunits in the 4-start helix. Thus, β 2AR may bind to individual pilin subunits but may also recognize a conformational epitope spanning two subunits.

Pilin subunits are connected in the Nm T4P by contacts between the globular domains, between the globular domains and the α 1s, and between the α 1s themselves. The staggered globular domains along the 1-start helix have limited contact, between the β 3– β 4 loop on one subunit and the $\alpha\beta$ -loop on the next (Fig. 4c).

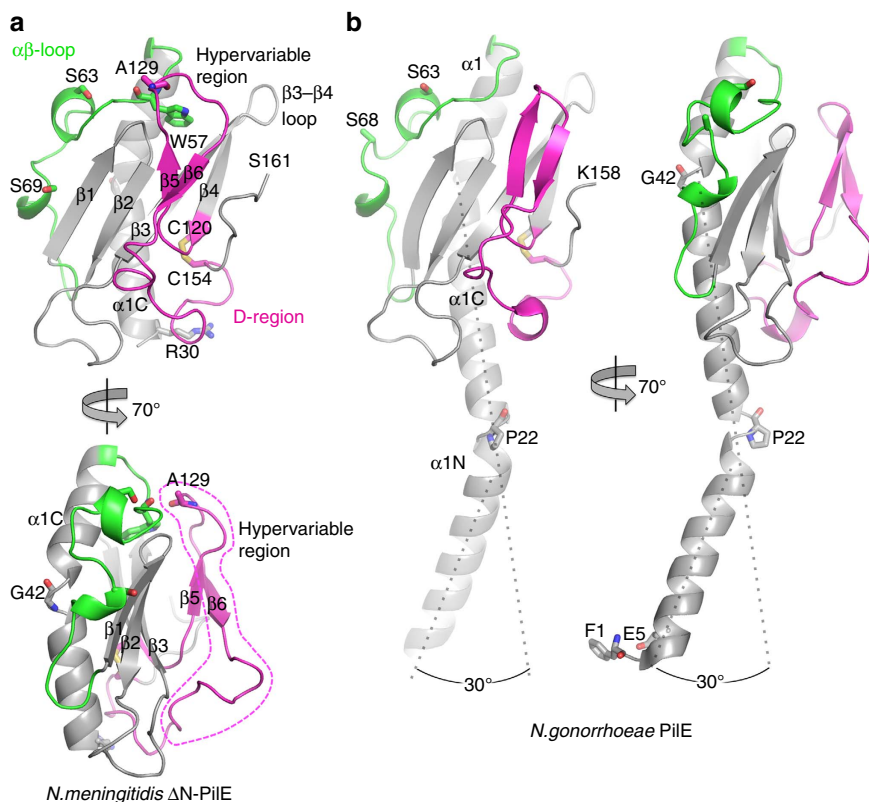


Figure 2 | X-ray crystal structure of *N. meningitidis* Δ N-PilE and comparison with the full-length structure of Ng PilE. Two views of (a) Nm Δ N-PilE and (b) Ng PilE pilins are shown: a ‘surface view’ predicted to form the outer face of the T4P filament, and a 70° rotation. The $\alpha\beta$ loop is shown in green and the D-region is shown in magenta, with the hypervariable region within the D-region outlined in the lower panel. Secondary structures are indicated. Nm Δ N-PilE residues Ser63 and Ser69 are post-translationally modified in the native pilin, as are the corresponding Ser63 and Ser68 shown in the full-length Ng PilE structure. The Ng PilE N-terminal α -helix, α 1, is kinked at Pro22 and Gly42. The N-terminal half of α 1, α 1N, is absent in the Nm Δ N-PilE structure, but is identical in sequence and thus expected to share the same conformation as in Ng PilE.

The bottoms of each globular domain fit into a gap between two globular domains in the next turn of the 1-start helix: the β 2– β 3 loop of the upper subunit contacts the tip of α 1 of one of the lower subunits, and the D-region of the upper subunit contacts both the top of α 1C and the $\alpha\beta$ -loop of the other lower subunit (Fig. 4c). These interactions, mediated by mostly polar and charged residues, connect the globular domains in each consecutive turn of the 1-start helical strand, and would block antibody access the EYYLN epitope at the end of α 1C. The interactions in the core of the filament are more extensive and involve mainly hydrophobic residues. The primary contact points between the α 1s occur along the 1-start helical strand: the continuous α -helical segments α 1:24–41, which are an integral part of their respective globular domains, alternate along the 1-start helix of the pilus filament with the ordered segments of α 1N (residues 1–14) from subunits in the next turn up in the 1-start helix (Fig. 4d, e). Each α 1:1–14 inserts between two α 1:24–41s of the 1-start helical turn below it, contacting both α 1:24–41 and the globular domain for one of the subunits and α 1:24–41 alone for the adjacent subunit. The most N-terminal portion of α 1:1–14 extends to the helical turn below this one to contact the C-terminal residues of α 1 at the EYYLN epitope (Fig. 4e). Thus, each subunit contacts three consecutive turns of the 1-start helix—the top one via globular domain interactions, the one below that via α 1:1–14 interactions with α 1:24–41 and globular domains, and the one below that via α 1:1–14 interactions with the EYYLN epitope of α 1. The hydrophobic interactions in the α -helical core of the T4P provide the remarkable stability of the pili, which are resistant to heat and

chemical denaturation and require treatment with detergent in order to dissociate them¹⁴.

The α -helical core of the *N. meningitidis* T4P. In our Nm T4P model the α 1 segment 24–53 is curved but runs roughly parallel to the filament axis while α 1:1–14 is tilted with its N terminus oriented toward the centre of the filament (Fig. 5a–c). This orientation places the side chain of Glu5 in close proximity (<5 Å) to the N-terminal amine of Phe1 (Phe1:N) on the neighbouring α 1 in the 1-start helix, consistent with a salt bridge, which matches perfectly the well-defined channel connecting the rod-like densities at their termini (Fig. 5b,c). Glu5 is invariant in Type IV pilins and Type II secretion pseudopilins and is also present in most minor (pseudo)pilins. Although the Phe1–Glu5 salt bridge has been proposed previously to neutralize these charges in the hydrophobic core of the filament¹¹ and to drive subunit docking into a growing pilus⁹ this is the first structural evidence of such an interaction in a T4P. Neither the rod-like density for α 1, nor the connection between these densities, were resolved in the 12.5 Å Ng T4P structure⁹. Thr2 is also positioned to form an intermolecular hydrogen bond with Glu5. A hydroxyl-containing threonine or serine is conserved at position 2 and is the only polar amino-acid apart from Glu5 in the first 25 residues of the Type IV pilins. Glu5 is essential for efficient T4P assembly^{14,16–22} and Type II secretion pseudopilus assembly⁴³. We have proposed that Glu5 facilitates docking of incoming pilin subunits into the growing pilus through electrostatic interactions with Phe1:N of the preceding subunit, neutralizing these two charges in the otherwise hydrophobic environment of the inner

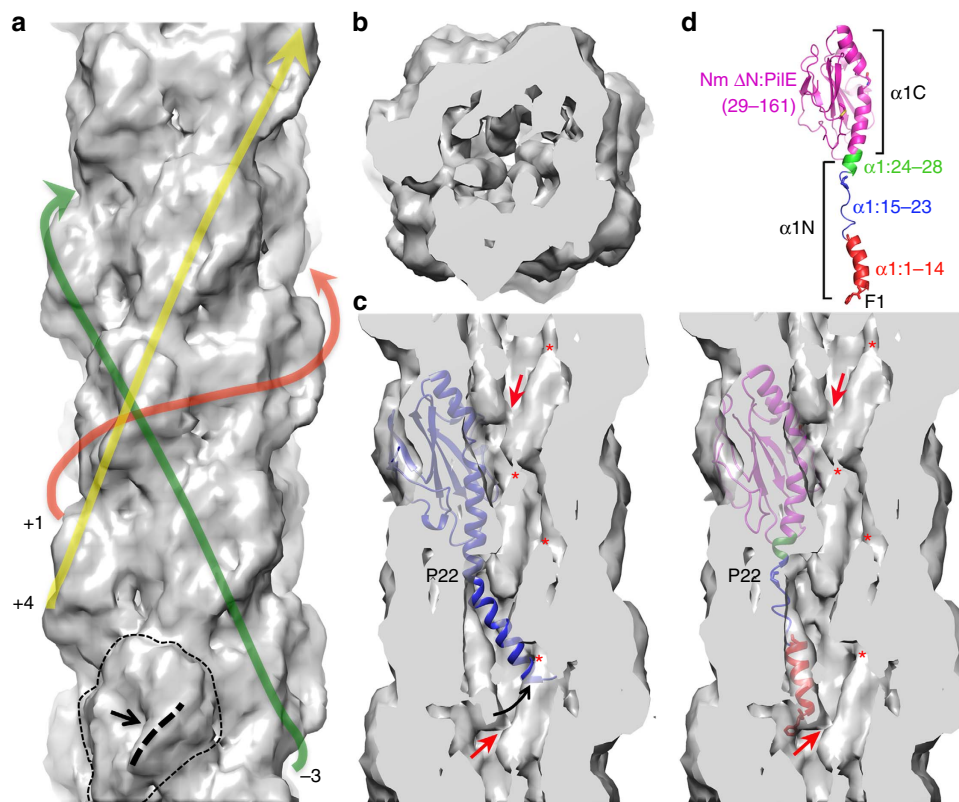


Figure 3 | CryoEM reconstruction of the *N. meningitidis* T4P at 6 Å resolution. (a) Side view of the Nm pilus cryoEM map showing the globular domain density and its connectivity in the right-handed 1-start helix (+1), the right-handed 4-start helix (+4) and the left-handed 3-start helix (−3). A single globular domain is outlined at the bottom of the map, with the ridge indicated with a thick dashed line and the central depression indicated with an arrow. (b) End view of a section of the cryoEM map showing the rod-like density corresponding to N-terminal α -helices. (c) Cross section of the Nm pilus reconstruction showing the rod-like α -helical density, the ends of which are connected near the central filament axis (red arrows). The full-length Ng PilE structure (2HI2) was fit as a rigid body into the globular domain density. The Pro22-induced kink results in the N-terminal α -helical segment completely missing the rod-like density. The rod-like density disappears just before it enters the globular domain density (red asterisks). (d) The Nm PilE structure was fit into the map in segments, as indicated. α 1N was modelled from the corresponding region in the Ng PilE crystal structure, with the helix melted in α 1:15–23, which straightens α 1.

Table 2 | Refinement statistics for the Ng T4P filament model.

<i>RMS deviations</i>	
Bonds (Å)	0.009
Angles (°)	1.04
<i>Ramachandran plot</i>	
Favoured (%)	75.5
Allowed (%)	23.9
Outliers (%)	0.6
Rotamer outliers (%)	0.0
C β deviations	0

RMS, root mean square.

membrane⁹ (Fig. 6a). This salt bridge appears to be maintained in the assembled pilus and may also contribute to filament stability.

The cryoEM map shows that α 1 is non-helical between the helix-breaking residues Gly14 and Pro22. The loss of α -helical order at α 1:15–23 compared with the all-helical conformation seen in the Ng PilE crystal structure lengthens α 1 and effectively removes the Pro22-induced kink. By eliminating the α -helical structure for α 1:15–23 we were able to place α 1:1–14 into the rod-like EM density, at a position quite different from that

predicted for Ng T4P (Fig. 3c,d). Yet the α -helices are not particularly tightly packed, leaving gaps in the filament core and a channel \sim 11 Å in diameter that winds through the filament (Figs 3b and 5a). This channel could accommodate flexibility in α 1:15–23 and in the pilus filament itself.

Discussion

Our 1.44 Å crystal structure of Nm Δ N-PilE, together with our \sim 6 Å resolution cryoEM reconstruction of the Nm T4P allowed us to generate a model for this pilus that closely resembles our earlier 12.5 Å Ng T4P structure (Supplementary Fig. 2) but reveals new structural features that inform pilus biology. The non-helical conformation revealed for residues 15–23 of α 1 is surprising given that this region is α -helical not only in the Ng PilE monomer structure but also in the other full-length Type IV pilin structures from *Pseudomonas aeruginosa*⁸, *Dichelobacter nodosus*¹⁰ and *G. sulfurreducens*¹² all of which possess S-shaped α -helices with kinks at Pro22 and Gly/Pro42. These full-length Type IV pilin structures were obtained by dissociating purified pili into pilin subunits with the detergent octyl β -D-glucopyranoside (β OG), which disrupts hydrophobic interactions and solubilizes α 1N. In bacteria α 1N is anchored in the inner membrane prior to pilus assembly¹³. The α -helical conformation would shield the polar nitrogens and oxygens in the α 1N backbone from the hydrophobic phase of the lipid bilayer

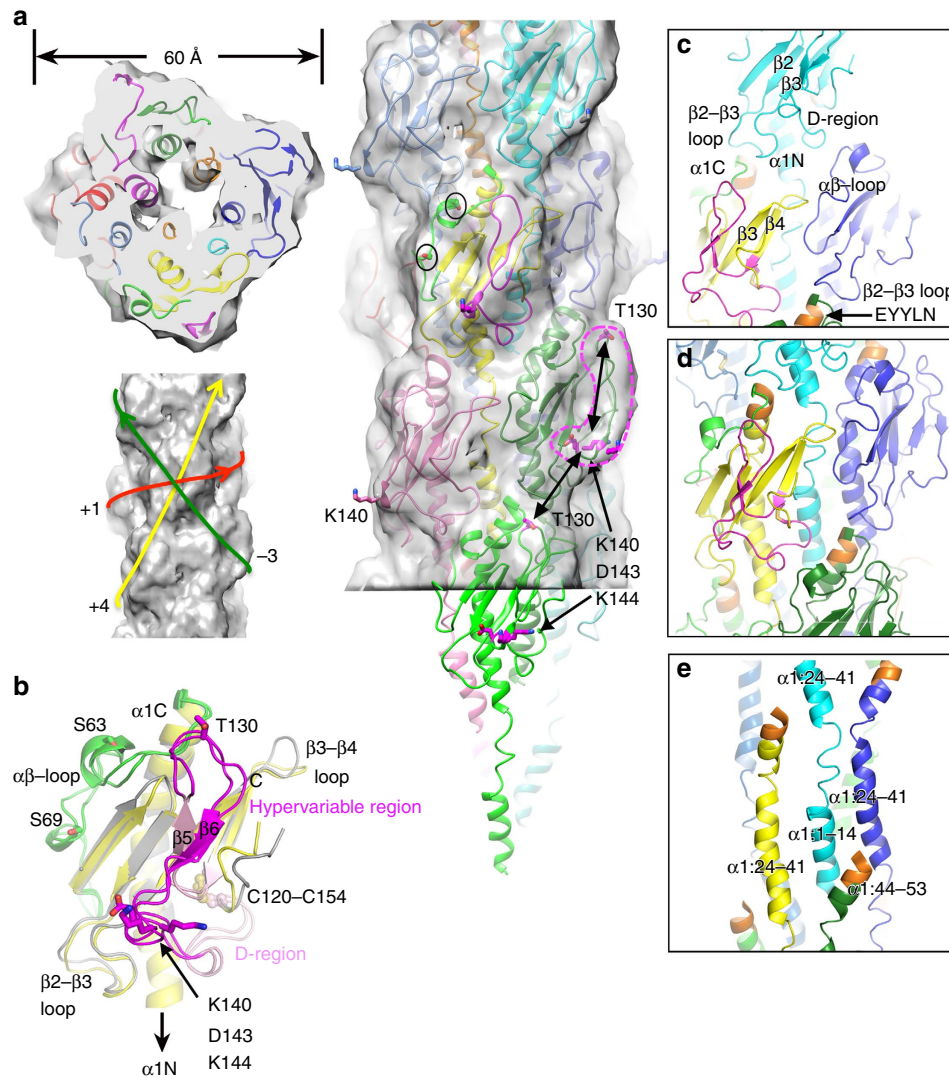


Figure 4 | Structure of the *N. meningitidis* T4P. (a) End and side view of the Nm T4P model fit into the cryoEM density, with each subunit shown in a different colour. In the side view the central subunit is coloured yellow with the $\alpha\beta$ -loop (residues 54–79) in green and the D-region (120–154) in magenta. Circled residues Ser63 and Ser69 within the $\alpha\beta$ -loop are post-translationally modified in the native T4P but these modifications are not resolved in the cryoEM reconstruction. The hypervariable region (127–146) within the D-region forms a ridge on the filament surface, indicated by the broken magenta line for one subunit. Residues Thr130, Lys140, Asp143 and Lys144 within the hypervariable ridge in this subunit and the adjacent green subunit are shown in stick representation with carbon atoms coloured magenta. These two β 2AR interaction sites are spaced equidistant apart (~ 26 Å) within a subunit and between subunits, as indicated by the double-headed arrows. The connectivity of the subunits is shown on the left below the end view. (b) Superposition of Nm Δ N-PilE before (grey, green and magenta) and after refinement in the pilus model (yellow, green and magenta). The D-region is coloured light pink and the hypervariable ridge within the D-region is coloured magenta. (c) Globular domain interactions shown from the perspective of the central subunit coloured as in (a), with the EYYLN epitope coloured orange. (d) The globular domains and their corresponding α 1:24–41 segments follow the +1-start helix and sandwich between them α 1:1–14 from subunits in the preceding turn of the +1-start helix. (e) Interactions among α 1s as shown in d but with residues 54–161 of the globular domains removed for clarity. α 1 segments are labelled.

(and also from the acyl chains of β OG during crystal growth). Thus, the melting of the helix at α 1:15–23 appears to be induced on integration of the pilin subunits into the pilus filament, perhaps to facilitate packing of α 1N (Fig. 6a). The conserved helix-breaking residues Gly14 and Pro22 may destabilize the α -helical secondary structure in this region, allowing it to unfold during pilus assembly. Interestingly the Type II secretion pseudopilins also have Gly14 and Pro22 (Fig. 1b) and thus may also adopt a non-helical conformation in this region within the pseudopilus. Similarly, although the Type IVb pilins lack the proline at position 22 they have glycines at positions 11, 14 and 19, which may destabilize this region in a manner similar to that of Gly14/Pro22. In contrast, archaeal flagellins contain an N

terminus that is homologous to α 1N in the Type IV pilins⁴⁴ but possess no proline in this segment, and glycines are not in conserved positions (Fig. 1b). A ~ 4 Å resolution cryoEM reconstruction of an archaeal flagellar-like filament from *Ignioccus hospitalis* was recently determined, which shows well-defined density corresponding to a straight, fully α -helical α 1N (ref. 45). Thus, the loss of helical order seen for Nm T4P may be a shared feature of the T4P and Type II secretion pseudopili but is not necessarily a universal feature of filament-forming proteins containing a Type IV pilin N-terminal domain.

The new Nm T4P model with its non-helical α 1 segment provides a molecular basis with which to understand the reversible force-dependent polymorphism observed for both

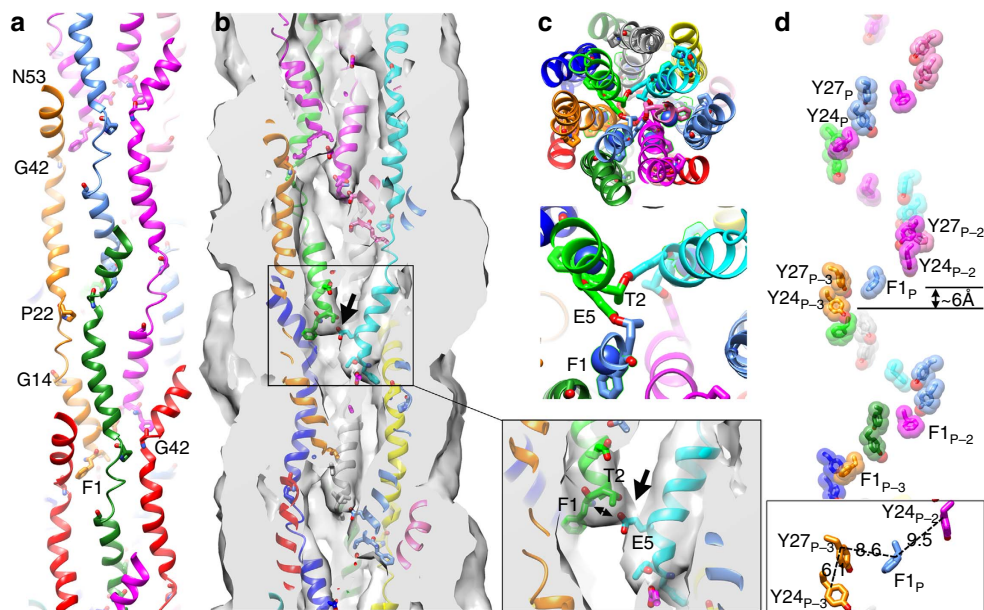


Figure 5 | Conformation and interactions among the N-terminal α -helices of the Nm T4P. (a) Side view of the α 1 segments only (residues 1–53) from the outside of the pilus, with Phe1, Glu5, Gly14, Pro22 and Gly42 shown in stick representation. (b) Cross-section of the α 1s in the cryoEM map. The interaction between the Glu5 side chain on one subunit and Phe1:N and the Thr2 side chain in the adjacent subunit in the 1-start helix is shown enlarged. The arrow points to the electron density corresponding to these contacts. The Phe1 side chain interacts with α 1C in the globular domain of an adjacent subunit. (c) End view of the α 1 core with a close-up of the interactions between Glu5 and Thr2 and Phe1:N (shown as a blue sphere). (d) Positions of the aromatic side chains of conserved residues Phe1, Tyr24 and Tyr27, all on α 1. Residues are numbered according to the position of their corresponding subunit or protomer, Pn, relative to the central subunit P (light blue). The Phe1 side chain is located between Tyr24/27 pairs on adjacent α 1s in the +1 helix, resulting in a continuous band of aromatic side chains that winds up the filament axis. These residues are implicated in electron transfer for the conductive *G. sulfurreducens* T4P^{48,49}. C γ –C γ distances for the final Nm T4P model are shown in the inset, although their precise positions are not known with certainty due to the limited resolution of the reconstruction.

Nm and Ng T4P^{29,32}. Ng T4P can be stretched to approximately three times their length when subjected to forces of ~ 100 pN, with a corresponding narrowing of the filament diameter²⁹. This force-induced conformational change exposes the EYYLN epitope at the end of α 1, which is normally buried in the pilus and only accessible at the tip (Figs 4c–e and 6). Similar exposure of this epitope is induced for Nm T4P upon binding to endothelial cells³². The mechanism by which Nm and Ng T4P can extend in a reversible manner was not apparent from the lower resolution Ng T4P model, in which the α 1s are all-helical and twisted around each other in the filament core⁹. The new Nm T4P model can be envisioned as a coil-like structure: each turn of the coil, which follows the 1-start helical path, is comprised of the globular domains connected by a small number of electrostatic/polar interactions and by extensive hydrophobic interactions with intervening α 1Ns (α 1:1–14) from the subunits in the next turn of the coil; each consecutive turn of the coil is held together axially by electrostatic and polar interactions between the globular domains and by α 1, which acts as a tether between each turn (Figs 4d,e and 6b, left panel). Shear forces on the pili may disrupt the weaker axial interactions between globular domains in consecutive turns of the coil, and extend residues α 1:15–23, stretching the pilus while maintaining the lateral interactions between globular domains, α 1:24–41 and α 1:1–14 along the coil (Fig. 6b, right panel). Thus, force would produce a spring-like motion separating the coils to elongate the pilus. Such a motion was described recently for the P pilus of the donor chaperone pilus family based on the 3.8 Å resolution cryoEM reconstruction⁴⁶. The architecture of the P pilus is markedly different from that of the T4P: elongated P pilin subunits are connected along the coils by donor-strand exchange of their N-terminal extensions, which insert into a groove in the next

subunit to complete an Ig fold⁴⁷; polar interactions hold the coils of the P pili together in the axial direction. Yet P pili, like the Nm and Ng T4P, can extend under force in a reversible spring-like manner, providing an interesting example of convergent evolution.

In our Nm T4P model α 1:15–23 spans ~ 18 Å. In a fully extended conformation these nine residues could potentially span ~ 32 Å, which would take the axial rise per subunit from 10.3 Å to ~ 24 Å, an increase of $\sim 230\%$. The melting of a few residues flanking 15–23 could further increase the filament length. Such an extension might separate the globular domains between consecutive turns of the coil enough for antibody to access to the EYYLN epitope, while maintaining the lateral hydrophobic interactions along the coil, between the globular domains, α 1:24–41 and α 1:1–14. Whereas the accompanying increase in rise per subunit can occur in the P pili by simply tilting the subunits, the more complex interactions holding the Type IV pilins may also shift relative to each other, changing the register of the α 1 interactions to increase the rise per subunit, transiently resulting in thinner longer pili. Upon release of force, α 1N would collapse to the more compact and stable conformation seen in the Nm T4P model and interactions between the coils would reform. This conformational elasticity would allow *N. meningitidis* to remain attached via T4P to endothelial cells in the brain vasculature, and *N. gonorrhoeae* cells to remain attached to the lining of the urethra under shear forces from blood and urine flow, respectively. Of note, the force-induced stretching of Nm T4P would separate the β 2AR-binding residue Thr130 from the Lys140/Asp143/Lys144 patch in adjacent subunits (Fig. 4b). Such a change may provide a signal to activate β 2AR and cortical plaque formation, leading to loosening of the endothelial cell junctions and opening of the blood brain barrier. The conformational flexibility of the Nm T4P is likely

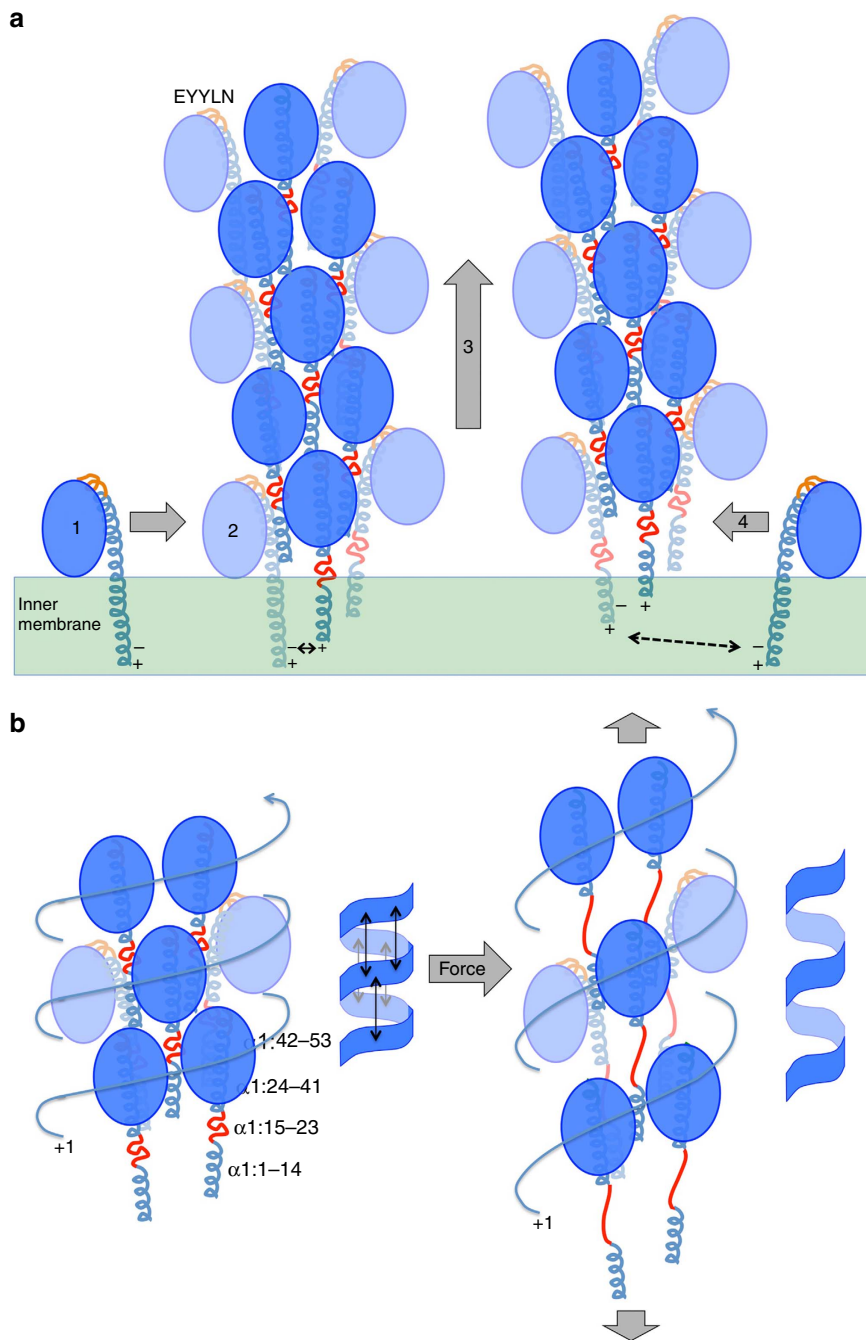


Figure 6 | Models for Type IV pilus assembly and force-induced conformational change. (a) T4P assembly model. (1) Before their incorporation into pilus filaments pilin subunits are anchored in the inner membrane with $\alpha 1$ in an all-helical conformation to shield backbone oxygens and nitrogens from the acyl phase of the lipid bilayer. (2) Pilin subunits dock into a growing pilus filament, attracted in part by charge complementarity between Glu5, represented by the $(-)$ charge, and the positively charged N-terminal amine $(+)$ on the terminal subunit in the growing pilus. (3) The pilus filament is extruded out of the membrane a short distance by the pilus assembly machinery, opening up a gap at the base of the pilus for a new subunit to dock. As the newly added pilin is extruded out of the inner membrane $\alpha 1:15-23$ (red) melts in order for $\alpha 1:1-14$ to pack into the filament core in an α -helical conformation. (4) Another subunit docks into the gap at the base of the pilus. The EYYLN epitope at the top of $\alpha 1$ is shown in orange. This epitope is exposed at the tip of the pilus and buried along its length. (b) Model for the force-induced conformational change of Nm and Ng T4P. Left panel: in its relaxed T4P conformation subunits are held together by lateral interactions between the globular domains along the $+1$ -start helix and alternating $\alpha 1$ Ns ($\alpha 1:1-14$) from the next turn up, as well as by axial interactions among the globular domains in consecutive turns of the $+1$ -start helix (represented by the double-headed arrows in the schematic of the coil). The central portion of $\alpha 1$, $\alpha 1:15-23$ (red), is non-helical but compact. The EYYLN epitope (orange) is only exposed at the tip of the pilus. Right panel: under stress, the axial interactions are disrupted and $\alpha 1:15-23$ becomes fully extended but the lateral interactions between the globular domains and $\alpha 1:1-14$ are maintained for the most part, allowing a spring-like extension of the pilus to expose the EYYLN epitope all along its length.

responsible for the structural heterogeneity observed during processing of the cryoEM images, which precluded a higher resolution reconstruction.

The Nm T4P structure may also be relevant in considering the mechanism for charge transfer in the related T4P from *G. sulfurreducens*. The *G. sulfurreducens* Type IV pilin is unique

in its absence of a globular domain: this 61 amino-acid pilin has an extended curved $\alpha 1$, as seen for Nm T4P, followed by an unstructured 8 amino-acid C terminus¹². This pilin shares 50% identity with Nm PilE in its N-terminal 30 amino acids, including Gly14 and Pro22 (Fig. 1b), thus it may also have a non-helical $\alpha 1$ segment when incorporated into a pilus. The *G. sulfurreducens* pilin contains 6 aromatic residues, Phe1, Tyr24, Tyr27, Tyr32, Phe51 and Tyr57, five of which are also present in Nm PilE. These residues are implicated in charge conduction in *G. sulfurreducens* T4P, as a mutant, Aro-5, with alanine substitutions for all aromatics except Phe1, makes pili but shows a 10-fold reduction in conductivity^{36,48,49}. The authors proposed metallic-like charge conductivity through closely spaced π - π stacked aromatic side chains, similar to electron transport through polyaniline or polyacetylene nanostructures⁴⁸. This model is supported by X-ray microdiffraction data for wild type conductive *G. sulfurreducens* T4P, which show a 3.2 Å peak representative of a repeating feature within the pilus; this peak is absent in the Aro-5 mutant³⁵. Since the spacing of the aromatic residues in existing T4P models^{8,9,14} is considerably larger than 3.2 Å, new computational models for the *G. sulfurreducens* T4P have been proposed that bring the core aromatic residues Phe1, Tyr24 and Tyr27 within π - π stacking distance (3–4 Å) to facilitate long-range electron transport through the pilus^{35,50}. Such energy-minimized models have a comparable rise to Nm T4P (~10 Å) but a much smaller twist (55–60°) and are more compact⁵⁰. While feasible, these models assume an all-helical $\alpha 1$. In our Nm T4P model with its non-helical $\alpha 1$ segment, the aromatic residues are not within π - π stacking distance, with most being >8 Å away (C γ -C γ) from their closest neighbour. Phe1, Tyr24 and Tyr27 form an aromatic band that spirals up the filament axis (Fig. 5d), whereas residues 32, 51 and 57, corresponding to the remaining aromatic amino acids in the *G. sulfurreducens* pilin, occupy more peripheral positions. Phe1 lies at approximately the same level along the Nm T4P filament axis as the Tyr27 of three subunits preceding (protomers P and P-3, respectively) and ~6 Å from Tyr24 (Fig. 5d), distances that are incompatible with π orbital overlap and the 3.2 Å diffraction peak seen for *G. sulfurreducens* T4P. The spacing of the aromatic side chains is constrained in Nm and Ng T4P by the presence of the globular domain, which places a lower limit on the subunit rise and rotation. The absence of a globular domain for the *G. sulfurreducens* Type IV pilins means that they can pack more closely in the pilus, with smaller rise and rotation values. These parameters, together with a non-helical, partially extended portion of $\alpha 1$, may provide more realistic *G. sulfurreducens* T4P computational models that aromatics except Phe1, Tyr24 and Tyr27, and perhaps other aromatic side chains, within 3–4 Å of each other to form a continuous chain of π - π stacked aromatic side chains for charge transfer. Interestingly, reduction of the solution pH from 10.5 to 2 results in a 100-fold increase in electrical conductivity for *G. sulfurreducens* T4P and a corresponding increase in the intensity of the 3.2 Å diffraction peak³⁵. A possible explanation for this apparent increase in order is that the low pH disrupts the Phe1-Glu5 salt bridge, freeing the Phe1 side chain to optimize its orientation for charge transfer.

In conclusion, the 6 Å structure of the Nm T4P provides a framework for understanding Nm pilus interactions with host cell receptors as well as more general aspects of T4P biology including assembly, function and biophysical properties. The highly conserved T4P N-terminal domain is all-helical in X-ray crystal structures of full-length Type IV pilins, which most likely represents its state in the inner membrane. On the basis of these crystal structures and low resolution EM reconstructions it has been assumed until now that $\alpha 1$ is all α -helical in the intact pilus as well. We have shown that the N-terminal segment is actually

partially melted in the assembled pilus. The melting of this region helps to explain pilus heterogeneity, flexibility and elasticity, including T4P's ability to stretch under force, and in the case of *G. sulfurreducens* T4P, to conduct charge. N-terminal sequence similarity between Nm PilE and other Type IV pilins and Type II secretion pseudopilins suggest that this $\alpha 1$ N melting may be a conserved feature, yet one that does not extend to the archaeal flagellins. The Nm T4P cryoEM reconstruction shows the limitations of secondary structure predictions, which can never be more than 80–90% accurate as they fail to account for contextual influences on protein structure. It also illustrates the value of obtaining the highest resolution possible for macromolecular assemblies, as key structural features can be missed with rigid body fitting of atomic structures of isolated subunits. Such features can have important biological implications for the protein complexes.

Methods

N. meningitidis PilE expression and purification. The gene fragment encoding PilE residues 29–161 (Δ N-PilE) was cloned from genomic DNA of *N. meningitidis* 8013 (high adhesive strain, SB)³⁷ using the primers Nm-pilE-EcoRI-fpcr (5'-CGG AATTCGCCCGCGCACAAAGTTCCGAAGCCATCCT-3') and Nm-pilE-PstI-rpcr (5'AACTGCAGTTAGCTGGCAGATGAATCATCGCGGCAGGT-3') and inserted into the pMAL-p2x plasmid (NEB) at the EcoRI and PstI cloning sites. The *pilE* gene was transferred into the pET15b vector (Novagen) restriction sites NdeI and BamHI using primers PilE-FP (5'-GCAATTCCATATGGCCCGCGCA CAAGTTTCC-3') and PilE-RP (5'-CCGCGGATCCTTAGCTGGCAGATGAATC ATCGC-3'). pET15b-*pilE*, which encodes an N-terminal His-tag, was transformed into *E. coli* BL21(DE3) SHuffle strain (NEB) and grown at 16 °C for 22 hrs in LB, 0.4 mM IPTG. Cells were lysed by sonication in lysis buffer (20 mM Tris-HCl, pH 8, lysozyme, 1 mg ml⁻¹, EDTA-free protease inhibitor (Roche)) and cell debris was removed by centrifugation. The lysate was loaded onto a Ni-NTA column and bound His- Δ N-PilE was eluted using elution buffer (50 mM Tris-HCl, pH 8, 100 mM NaCl, 250 mM imidazole) then dialysed in the presence of thrombin to simultaneously remove the imidazole and the His-tag. Δ N-PilE was further purified by size exclusion chromatography using a HiPrep 26/60 Sephacryl S-100 HR column (GE Healthcare) in buffer containing 20 mM Tris-HCl, pH 7.4, 100 mM NaCl. Fractions containing Δ N-PilE were pooled, concentrated to 15 mg ml⁻¹ using a stirred-cell concentrator (Millipore) and flash-frozen.

Δ N-PilE crystallization, data collection and refinement. Δ N-PilE crystals were grown by the hanging drop vapour diffusion method at 293 K. Initial crystallization conditions were obtained from the high throughput screening laboratory at the Hauptman-Woodward Medical Research Institute⁵¹ then optimized in-house. Diffraction-quality crystals grew in 4 μ l drops containing a 1:1 ratio of protein (15 mg ml⁻¹) and reservoir solution (0.1 M ammonium sulfate, 0.1 M MES pH 6, 34% (W/V) PEG 4,000). The needle shaped crystals were cryocooled in mother liquor with 30% (v/v) glycerol for storage and transport to the Stanford Synchrotron Radiation Lightsource (SSRL) for X-ray diffraction data collection.

Diffraction data for Δ N-PilE were collected at the SSRL Beamline 7.1 by remote access using Blu-Ice software⁵². Raw data were processed and scaled and structure factor amplitudes were determined by data processing suite XDS⁵³. Matthews coefficient calculations using the CCP4 program MATTHEWS_COEF^{54,55} indicated that the asymmetric unit contains one Δ N-PilE molecule with 39.3% solvent content. The crystal structure was solved by the molecular replacement method using the program PHASER⁵⁶ in CCP4i^{54,57}. The Nm PilE crystal structure (PDB ID 2HI2⁹), with the N-terminal 29 residues removed, was used as the model. Molecular replacement yielded an unambiguous solution with z-scores RFZ = 9.8, and TFZ = 14.5. The model residues were changed to those of Nm PilE in COOT⁵⁸ where necessary and rigid body refinement was carried out followed by 20 cycles of restrained refinement using REFMAC⁵⁹, which brought R_{work} and R_{free} to 0.271 and 0.317, respectively. The Δ N-PilE model was examined and adjusted in COOT using difference maps. The modified model was further refined using the 'Improvement of maps by atoms update and refinement' tool in ARP/wARP⁶⁰, bringing the R_{work} to 0.197 and the R_{free} to 0.266. A composite annealed omit map was calculated using CNS⁶¹ and all the residues and water oxygens were validated with the omit map, to give R_{work} of 0.211 and R_{free} of 0.238. At this point the coordinates were validated and deposited in the protein data bank (PDB ID 4XNP). However, after employing the PHENIX suite⁶² to refine the Nm T4P model we used this program to re-refined the Δ N-PilE structure with options 'Automatically add hydrogens to model' and 'Update waters', reducing the R-factors to 0.187 (R_{free}) and 0.210 (R_{free}). These Δ N-PilE coordinates were deposited to the PDB under the accession number 5JW8. Data collection and refinement statistics are reported in Table 1.

Preparation of *N. meningitidis* T4P for cryoEM. *N. meningitidis* 8013 cells were grown on GCB plates⁶³, resuspended in solubilization buffer (20 mM

ethanolamine, pH 10.5) and vortexed to shear the pili from the cells. Cells were removed from the sheared sample by two rounds of centrifugation at 4,000g and pili were precipitated by the addition of ammonium sulfate to 10% saturation and 16 h incubation at 16 °C. Pili were collected by centrifugation (13,000g, 60 min, 4 °C) and resuspended in solubilization buffer. A second round of purification was performed by addition of ammonium sulfate to 10% saturation and precipitation. The final protein concentration was 0.4 µg µl in 20 mM ethanolamine, pH 10.5.

CryoEM and image processing. Samples (2 µl) were applied to plasma-cleaned lacey carbon grids and vitrified using a VitroBot Mark IV (FEI, Inc.). Images were collected at an operating voltage of 300 keV on an FEI Titan Krios equipped with a Falcon 2 direct electron detector. The magnification used provided a sampling of 1.05 Å per pixel. A total of 2,295 images were collected from a single grid using the EPU automated system on the Krios, and these were reduced to 541 images after discarding those with no filaments or extensively aggregated filaments, poor contrast transfer function (CTF) and so on. Images were stored containing seven ‘chunks’, where each chunk represents a set of frames corresponding to a dose of ~20 electrons per Å². The full dose image stack was used for the estimation of the CTF, using CTFIND3 (ref. 64), as well as for boxing filaments using the e2helixboxer routine within EMAN2 (ref. 65). The SPIDER software package⁶⁶ was used for almost all other operations. Phase reversals in the images were corrected by multiplying each image by the calculated CTF, which is a Wiener filter in the limit of a very low SNR.

Approximately 100,000 overlapping pilus segments, each 384 px long and shifted by 15 px (~1.5 times the axial rise per subunit) were cut from the long boxes, and these were reduced to 69,621 after discarding those with a large out-of-plane tilt. The IHRSR method⁴¹ was used to generate a global reconstruction, and this was then deformed corresponding to different values of the axial rise and rotation (twist) of the subunits to generate an ensemble of structures used for multi-reference sorting. This sorting suggested that most structural variability existed within the twist, and a new sorting was done keeping the axial rise fixed at 10.3 Å with a twist ranging from 98.8 to 102.8°. The central bin from this sorting, corresponding to a rotation of 100.8°, contained 15,586 segments which were used for the final reconstruction. The amplitudes of the reconstruction were corrected for the CTF by dividing them by the sum of the squared CTFs, since they had been multiplied by the CTF twice: once by the microscope, and once computationally in the phase corrections. The reconstruction was filtered to 5.0 Å and sharpened with a negative B-factor of 150 for preparation of figures.

Atomic model of the Nm T4P. The Nm ΔN-PilE structure (residues 29–161) was docked into the pilus reconstruction using the ‘Fit in Map’ tool in Chimera⁶⁷. Residue positions in the tight loop at the C-terminal end of the αβ-loop (73–78) and the β3–β4 loop (112–115) were adjusted to optimize their fit in the map. Next, the full-length Ng PilE crystal structure was superimposed on Nm ΔN-PilE to obtain coordinates for part of the protruding segment of α1, α1N. This superposition provided coordinates for α1N residues 24–28 but residues N-terminal to these fit poorly into the cryoEM map due to the kink induced by Pro22, which directs most of α1N away from the rod-like density in the filament core. COOT⁵⁸ was used to fit varying lengths of the most N-terminal portion of the Ng PilE structure into the rod-like density (for example, residues 1–12, 1–13, 2–13, 2–14 and so on). The angle of rotation along the helical axis of this N-terminal α-helical segment was varied to minimize the distance between the Glu5 side chain and the Phe1:N in adjacent subunits in the +1 helix. Residues linking this α-helical segment to α1:24–28 were built in an extended conformation due to the weak density in this region. In models where residues 1 and 2 were included in the rod-like density, ideal α-helical phi/psi angles were imposed using COOT as these residues are extended in the Ng PilE structure. Bond lengths and angles of this full-length Nm PilE subunit starting model were idealized using REFMAC⁵⁹. This PilE model, docked into the EM density, was designated Subunit A. A second PilE model was fit into the adjacent subunit density and designated Subunit B. The symmetry operation (rise and rotation) relating these two subunits was determined by LSQKAB in CCP4, and used to generate Nm T4P models of 10 or 21 subunits with CCP4 PDBSET. The cryoEM map in BRX format was converted into CCP4 format using MAPMAN, and the Nm T4P models were refined against this map using the PHENIX suite⁶². B-factors were fixed during refinement due to the limited resolution of the reconstruction. Refined models were examined within the cryoEM map in Chimera to identify steric clashes between subunits, which were removed by altering side chain conformations and then additional refinement cycles were run. The modelling proceeded iteratively, with each new model examined in CHIMERA, modified to improve its fit in the map, minimize steric clashes and the Phe1:N-Glu5 distance followed by refinement cycles. Refinement statistics are shown in Table 2.

The resolution of the final reconstruction was estimated at ~6 Å by Fourier Shell Correlation (FSC) between the map and the atomic model (Supplementary Fig. 3). This avoids several problems with the traditional map:map FSC, such as the fact that it can be completely artifactual for helical structures⁶⁸.

Data availability. The Nm ΔN-PilE was deposited in the PDB under accession number 5JW8. The Nm T4P reconstruction was deposited in the Electron

Microscopy Data Bank under accession number EMD-8287, and the corresponding atomic filament model was deposited in the PDB under accession number 5KUA. The data that support the findings of this study are available from the corresponding authors on request.

References

- Coureur, M. *et al.* Meningococcal type IV pili recruit the polarity complex to cross the brain endothelium. *Science* **325**, 83–87 (2009).
- Dupin, N. *et al.* Chronic meningococemia cutaneous lesions involve meningococcal perivascular invasion through the remodeling of endothelial barriers. *Clin. Infect. Dis.* **54**, 1162–1165 (2012).
- Pron, B. *et al.* Interaction of *Neisseria meningitidis* with the components of the blood-brain barrier correlates with an increased expression of PilC. *J. Infect. Dis.* **176**, 1285–1292 (1997).
- Sotto, M. N., Langer, B., Hoshino-Shimizu, S. & de Brito, T. Pathogenesis of cutaneous lesions in acute meningococemia in humans: light, immunofluorescent, and electron microscopic studies of skin biopsy specimens. *J. Infect. Dis.* **133**, 506–514 (1976).
- Merz, A. J., Enns, C. A. & So, M. Type IV pili of pathogenic *Neisseriae* elicit cortical plaque formation in epithelial cells. *Mol. Microbiol.* **32**, 1316–1332 (1999).
- Bernard, S. C. *et al.* Pathogenic *Neisseria meningitidis* utilizes CD147 for vascular colonization. *Nat. Med.* **20**, 725–731 (2014).
- Coureur, M. *et al.* Meningococcus Hijacks a beta2-adrenoceptor/beta-Arrestin pathway to cross brain microvasculature endothelium. *Cell* **143**, 1149–1160 (2010).
- Craig, L. *et al.* Type IV pilin structure and assembly: X-ray and EM analyses of *Vibrio cholerae* toxin-coregulated pilus and *Pseudomonas aeruginosa* PAK pilin. *Mol. Cell* **11**, 1139–1150 (2003).
- Craig, L. *et al.* Type IV pilus structure by cryo-electron microscopy and crystallography: implications for pilus assembly and functions. *Mol. Cell* **23**, 651–662 (2006).
- Hartung, S. *et al.* Ultra-high resolution and full-length pilin structures with insights for filament assembly, pathogenic functions and vaccine potential. *J. Biol. Chem.* **286**, 44254–44265 (2011).
- Parge, H. E. *et al.* Structure of the fibre-forming protein pilin at 2.6 Å resolution. *Nature* **378**, 32–38 (1995).
- Reardon, P. N. & Mueller, K. T. Structure of the type IVa major pilin from the electrically conductive bacterial nanowires of *Geobacter sulfurreducens*. *J. Biol. Chem.* **288**, 29260–29266 (2013).
- Morand, P. C. *et al.* Type IV pilus retraction in pathogenic *Neisseria* is regulated by the PilC proteins. *EMBO J.* **23**, 2009–2017 (2004).
- Li, J., Egelman, E. H. & Craig, L. Structure of the *Vibrio cholerae* Type IVb pilus and stability comparison with the *Neisseria gonorrhoeae* Type IVa pilus. *J. Mol. Biol.* **418**, 47–64 (2012).
- Li, J. *et al.* *Vibrio cholerae* toxin-coregulated pilus structure analyzed by hydrogen/deuterium exchange mass spectrometry. *Structure* **16**, 137–148 (2008).
- Aas, F. E., Lovold, C. & Koomey, M. An inhibitor of DNA binding and uptake events dictates the proficiency of genetic transformation in *Neisseria gonorrhoeae*: mechanism of action and links to Type IV pilus expression. *Mol. Microbiol.* **46**, 1441–1450 (2002).
- Aas, F. E. *et al.* Substitutions in the N-terminal alpha helical spine of *Neisseria gonorrhoeae* pilin affect Type IV pilus assembly, dynamics and associated functions. *Mol. Microbiol.* **63**, 69–85 (2007).
- Hobbs, M., Collie, E. S., Free, P. D., Livingston, S. P. & Mattick, J. S. PilS and PilR, a two-component transcriptional regulatory system controlling expression of type 4 fimbriae in *Pseudomonas aeruginosa*. *Mol. Microbiol.* **7**, 669–682 (1993).
- Horiuchi, T. & Komano, T. Mutational analysis of plasmid R64 thin pilus prepilin: the entire prepilin sequence is required for processing by type IV prepilin peptidase. *J. Bacteriol.* **180**, 4613–4620 (1998).
- Kirn, T. J., Lafferty, M. J., Sandoe, C. M. & Taylor, R. K. Delineation of pilin domains required for bacterial association into microcolonies and intestinal colonization by *Vibrio cholerae*. *Mol. Microbiol.* **35**, 896–910 (2000).
- Pasloske, B. L. & Paranchych, W. The expression of mutant pilins in *Pseudomonas aeruginosa*: fifth position glutamate affects pilin methylation. *Mol. Microbiol.* **2**, 489–495 (1988).
- Strom, M. S. & Lory, S. Amino acid substitutions in pilin of *Pseudomonas aeruginosa*. Effect on leader peptide cleavage, amino-terminal methylation, and pilus assembly. *J. Biol. Chem.* **266**, 1656–1664 (1991).
- Craig, L., Pique, M. E. & Tainer, J. A. Type IV pilus structure and bacterial pathogenicity. *Nat. Rev. Microbiol.* **2**, 363–378 (2004).
- Gibbs, C. P. *et al.* Reassortment of pilin genes in *Neisseria gonorrhoeae* occurs by two distinct mechanisms. *Nature* **338**, 651–652 (1989).
- Potts, W. J. & Saunders, J. R. Nucleotide sequence of the structural gene for class I pilin from *Neisseria meningitidis*: homologues with the pilE locus of *Neisseria gonorrhoeae*. *Mol. Microbiol.* **2**, 647–653 (1988).

26. Seifert, H. S., Ajioka, R. S., Marchal, C., Sparling, P. F. & So, M. DNA transformation leads to pilin antigenic variation in *Neisseria gonorrhoeae*. *Nature* **336**, 392–395 (1988).
27. Maier, B., Potter, L., So, M., Seifert, H. S. & Sheetz, M. P. Single pilus motor forces exceed 100 pN. *Proc. Natl. Acad. Sci. USA* **99**, 16012–16017 (2002).
28. Merz, A. J., So, M. & Sheetz, M. P. Pilus retraction powers bacterial twitching motility. *Nature* **407**, 98–102 (2000).
29. Biais, N., Higashi, D. L., Bruijic, J., So, M. & Sheetz, M. P. Force-dependent polymorphism in type IV pili reveals hidden epitopes. *Proc. Natl. Acad. Sci. USA* **107**, 11358–11363 (2010).
30. Biais, N., Ladoux, B., Higashi, D., So, M. & Sheetz, M. Cooperative retraction of bundled type IV pili enables nanonewton force generation. *PLoS Biol.* **6**, e87 (2008).
31. Clausen, M., Jakovljevic, V., Sogaard-Andersen, L. & Maier, B. High-force generation is a conserved property of type IV pilus systems. *J. Bacteriol.* **191**, 4633–4638 (2009).
32. Brissac, T., Mikaty, G., Dumenil, G., Coureuil, M. & Nassif, X. The meningococcal minor pilin PilX is responsible for type IV pilus conformational changes associated with signaling to endothelial cells. *Infect. Immun.* **80**, 3297–3306 (2012).
33. Forest, K. T. *et al.* Assembly and antigenicity of the *Neisseria gonorrhoeae* pilus mapped with antibodies. *Infect. Immun.* **64**, 644–652 (1996).
34. Virji, M., Heckels, J. E., Potts, W. J., Hart, C. A. & Saunders, J. R. Identification of epitopes recognized by monoclonal antibodies SM1 and SM2 which react with all pili of *Neisseria gonorrhoeae* but which differentiate between two structural classes of pili expressed by *Neisseria meningitidis* and the distribution of their encoding sequences in the genomes of *Neisseria* spp. *J. Gen. Microbiol.* **135**, 3239–3251 (1989).
35. Malvankar, N. S. *et al.* Structural basis for metallic-like conductivity in microbial nanowires. *MBio* **6**, e00084 (2015).
36. Reguera, G. *et al.* Extracellular electron transfer via microbial nanowires. *Nature* **435**, 1098–1101 (2005).
37. Nassif, X. *et al.* Antigenic variation of pilin regulates adhesion of *Neisseria meningitidis* to human epithelial cells. *Mol. Microbiol.* **8**, 719–725 (1993).
38. Miller, F. *et al.* The hypervariable region of meningococcal major pilin PilE controls the host cell response via antigenic variation. *MBio* **5**, e01024–13 (2014).
39. Chamot-Rooke, J. *et al.* Posttranslational modification of pili upon cell contact triggers *N. meningitidis* dissemination. *Science* **331**, 778–782 (2011).
40. Chamot-Rooke, J. *et al.* Alternative *Neisseria* spp. type IV pilin glycosylation with a glyceramido acetamido trioxohexose residue. *Proc. Natl. Acad. Sci. USA* **104**, 14783–14788 (2007).
41. Egelman, E. H. A robust algorithm for the reconstruction of helical filaments using single-particle methods. *Ultramicroscopy* **85**, 225–234 (2000).
42. Marceau, M., Beretti, J. L. & Nassif, X. High adhesiveness of encapsulated *Neisseria meningitidis* to epithelial cells is associated with the formation of bundles of pili. *Mol. Microbiol.* **17**, 855–863 (1995).
43. Nivaskumar, M. *et al.* Pseudopilin residue E5 is essential for recruitment by the type 2 secretion system assembly platform. *Mol. Microbiol.* **101**, 924–941 (2016).
44. Bayley, D. P. & Jarrell, K. F. Further evidence to suggest that archaeal flagella are related to bacterial type IV pili. *J. Mol. Evol.* **46**, 370–373 (1998).
45. Braun, T. *et al.* Archaeal flagellin combines a bacterial type IV pilin domain with an Ig-like domain. *Proc. Natl. Acad. Sci. USA* **113**, 10352–10357 (2016).
46. Hospenthal, M. K. *et al.* Structure of a chaperone-usher pilus reveals the molecular basis of rod uncoiling. *Cell* **164**, 269–278 (2016).
47. Sauer, F. G., Pinkner, J. S., Waksman, G. & Hultgren, S. J. Chaperone priming of pilus subunits facilitates a topological transition that drives fiber formation. *Cell* **111**, 543–551 (2002).
48. Malvankar, N. S. *et al.* Tunable metallic-like conductivity in microbial nanowire networks. *Nat. Nanotechnol.* **6**, 573–579 (2011).
49. Vargas, M. *et al.* Aromatic amino acids required for pili conductivity and long-range extracellular electron transport in *Geobacter sulfurreducens*. *MBio* **4**, e00105–e00113 (2013).
50. Xiao, K. *et al.* Low energy atomic models suggesting a pilus structure that could account for electrical conductivity of *Geobacter sulfurreducens* pili. *Sci. Rep.* **6**, 23385 (2016).
51. Luft, J. R. *et al.* A deliberate approach to screening for initial crystallization conditions of biological macromolecules. *J. Struct. Biol.* **142**, 170–179 (2003).
52. Gonzales, A. *et al.* Web-Ice: integrated data collection and analysis for macromolecular crystallography. *Journal of Applied Crystallography* **41**, 176–184 (2008).
53. Kabsch, H. Automatic processing of rotation diffraction data from crystals of initially unknown symmetry and cell constants. *Journal of Applied Crystallography* **26**, 795–800 (1993).
54. Collaborative Computational Project. Number 4, 1994: The CCP4 Suite: Programs for Protein Crystallography. *Acta Crystallogr.* **D50**, 760–763 (1994).
55. Matthews, B. W. Solvent content of protein crystals. *J. Mol. Biol.* **33**, 491–497 (1968).
56. McCoy, A. J. *et al.* Phaser crystallographic software. *J. Appl. Crystallogr.* **40**, 658–674 (2007).
57. Potterton, E., Briggs, P., Turkenburg, M. & Dodson, E. A graphical user interface to the CCP4 program suite. *Acta. Cryst.* **D59**, 1131–1137 (2003).
58. Emsley, P. & Cowtan, K. Coot: model-building tools for molecular graphics. *Acta Crystallogr. D Biol. Crystallogr.* **60**, 2126–2132 (2004).
59. Murshudov, G. N., Vagin, A. A. & Dodson, E. J. Refinement of macromolecular structures by the maximum-likelihood method. *Acta Crystallogr. D Biol. Crystallogr.* **53**, 240–255 (1997).
60. Langer, G., Cohen, S. X., Lamzin, V. S. & Perrakis, A. Automated macromolecular model building for X-ray crystallography using ARP/wARP version 7. *Nat. Protoc.* **3**, 1171–1179 (2008).
61. Brunger, A. T. *et al.* Crystallography & NMR system: A new software suite for macromolecular structure determination. *Acta Crystallogr. D Biol. Crystallogr.* **54**(Pt 5): 905–921 (1998).
62. Adams, P. D. *et al.* PHENIX: a comprehensive Python-based system for macromolecular structure solution. *Acta Crystallogr. D Biol. Crystallogr.* **66**, 213–221 (2010).
63. Nassif, X., Puaoi, D. & So, M. Transposition of Tn1545-delta 3 in the pathogenic *Neisseria*: a genetic tool for mutagenesis. *J. Bacteriol.* **173**, 2147–2154 (1991).
64. Mindell, J. A. & Grigorieff, N. Accurate determination of local defocus and specimen tilt in electron microscopy. *J. Struct. Biol.* **142**, 334–347 (2003).
65. Tang, G. *et al.* EMAN2: an extensible image processing suite for electron microscopy. *J. Struct. Biol.* **157**, 38–46 (2007).
66. Frank, J. *et al.* SPIDER and WEB: processing and visualization of images in 3D electron microscopy and related fields. *J. Struct. Biol.* **116**, 190–199 (1996).
67. Pettersen, E. F. *et al.* UCSF chimera - a visualization system for exploratory research and analysis. *J. Comput. Chem.* **25**, 1605–1612 (2004).
68. Egelman, E. H. Ambiguities in helical reconstruction. *Elife* **3**, e04969 (2014).
69. Sievers, F. *et al.* Fast, scalable generation of high-quality protein multiple sequence alignments using Clustal Omega. *Mol. Syst. Biol.* **7**, 539 (2011).
70. Robert, X. & Gouet, P. Deciphering key features in protein structures with the new ENDscript server. *Nucleic Acids Res.* **42**, W320–W324 (2014).
71. Piepenbrink, K. H. *et al.* Structural and evolutionary analyses show unique stabilization strategies in the type IV pili of *Clostridium difficile*. *Structure* **23**, 385–396 (2015).

Acknowledgements

We thank Grace (Guixiang) Yang for expression and purification of ΔN-PilE and Pavel Afonine (Lawrence Berkeley National Laboratory) for assistance with Phenix during the construction of the Nm T4P model. This research was funded by CIHR grant MOP125959 and NSERC grant RGPIN312152 to L.C. and NIH EB001567 to E.H.E. The laboratory of XN is supported by INSERM, CNRS, Université Paris Descartes, the Agence Nationale de la Recherche and the Fondation pour la Recherche Médicale.

Author contributions

S.K. solved the ΔN-PilE crystal structure and generated and refined the Nm T4P model. M.C. and X.N. initiated the collaboration, cloned the *pilE* gene into pMal and purified Nm T4P for cryoEM. X.Y. performed the cryoEM and filament selection. E.H.E. performed the image analysis and T4P reconstruction and contributed to T4P model building. L.C. coordinated the project and guided the model building. L.C., S.K. and E.H.E. analysed the structures. E.H.E. and L.C. co-wrote the manuscript.

Additional information

Supplementary information accompanies this paper at <http://www.nature.com/naturecommunications>

Competing financial interests: The authors declare no competing financial interests.

Reprints and permission information is available online at <http://npg.nature.com/reprintsandpermissions/>

How to cite this article: Kolappan, S. *et al.* Structure of the *Neisseria meningitidis* Type IV pilus. *Nat. Commun.* **7**, 13015 doi: 10.1038/ncomms13015 (2016).



This work is licensed under a Creative Commons Attribution 4.0 International License. The images or other third party material in this article are included in the article's Creative Commons license, unless indicated otherwise in the credit line; if the material is not included under the Creative Commons license, users will need to obtain permission from the license holder to reproduce the material. To view a copy of this license, visit <http://creativecommons.org/licenses/by/4.0/>

© The Author(s) 2016